

PROBING EARLY STRUCTURE FORMATION WITH FAR-INFRARED BACKGROUND CORRELATIONS

LLOYD KNOX, ASANTHA COORAY, DANIEL EISENSTEIN¹

Department of Astronomy and Astrophysics, University of Chicago, Chicago, IL 60637, USA, email:
knox@flight.uchicago.edu, asante@oddjob.uchicago.edu, eisenste@oddjob.uchicago.edu

AND

ZOLTAN HAIMAN¹

Department of Astronomy, Princeton University, email: zoltan@astro.princeton.edu
To be submitted to ApJ

ABSTRACT

The large-scale structure of high-redshift galaxies produces correlated anisotropy in the far-infrared background (FIRB). In regions of the sky where the thermal emission from Galactic dust is well below average, these high-redshift correlations may be the most significant source of angular fluctuation power over a wide range of angular scales, from $\sim 7'$ to $\sim 3^\circ$, and frequencies, from ~ 400 to ~ 1000 GHz. The strength of this signal should allow detailed studies of the statistics of the FIRB fluctuations, including the shape of the angular power spectrum at a given frequency and the degree of coherence between FIRB maps at different frequencies. The FIRB correlations depend upon and hence constrain the redshift-dependent spectral energy distributions, number counts, and clustering bias of the galaxies and active nuclei that contribute to the background. We quantify the accuracy to which *Planck* and a newly proposed balloon-borne mission *EDGE* could constrain models of the high-redshift universe through the measurement of FIRB fluctuations. We conclude that the average bias of high-redshift galaxies could be measured to an accuracy of $\lesssim 1\%$ or, for example, separated into 4 redshift bins with $\sim 10\%$ accuracy.

Subject headings: cosmology: theory – cosmology: observation – cosmology: far infrared background – cosmic microwave background – galaxies: formation – galaxies: evolution

1. INTRODUCTION

The discovery of the cosmic far-infrared background (FIRB; Puget et al. 1996; Fixsen et al. 1998; Dwek et al. 1998; Schlegel et al. 1998; Lagache et al. 1999) and the determination of its spectrum have resulted in a new probe of structure formation in the high-redshift universe (e.g. Guiderdoni et al. 1998; Blain et al. 1999a; Haiman & Knox 2000). A compelling explanation for the background is that it results from the thermal emission of interstellar dust associated with high-redshift galaxies and heated by the internal optical and ultraviolet (UV) radiation from stars and to a lesser extent active galactic nuclei (AGN) (Stecker et al. 1977; Bond et al. 1986). Thus, the basic properties of the FIRB are sensitive to the role of galaxy formation and subsequent evolution.

Observing the FIRB at higher angular resolution and higher sensitivity than was done by the Far Infrared Absolute Spectrometer (FIRAS, Mather et al. (1999)) instrument on the Cosmic Background Explorer (*COBE*) satellite should reveal the presence of correlated fluctuations resulting from the correlations in the galaxies contributing to the background. Haiman and Knox (2000, hereafter HK00) used simplified semi-analytic models for the origin of the background flux to show that these correlated anisotropies have an amplitude that is roughly 10% of the mean, a level detectable with current technologies. The purpose of the present paper is to (1) spell out and quantify what one could learn from detailed observations of the FIRB correlations, (2) show that such detailed studies are possible due to the absence of other strong sources of fluctuation power in the relevant range of frequencies and

angular scales, and (3) show that FIRB anisotropy observations provide a powerful complement to direct high-angular resolution observations of the individual sources.

As we discuss in detail later, the background at different frequencies is composed of sources from differing ranges of redshifts. FIRB maps at multiple frequencies are therefore not expected to correlate perfectly with each other. We show how the shape of the FIRB angular power spectrum at different frequencies and the correlations between the maps can be used to determine physical properties of contributing high-redshift sources, in particular the product of the infrared emissivity of the sources and their bias relative to the dark matter density field. With assumptions about the source biasing and spectra, the infrared emissivity as a function of redshift can be converted to a measurement of the energy-production history of the universe, complementing current approaches involving optical and UV observations (e.g. Madau 1997; Madau et al. 1998). Conversely, one could combine FIRB anisotropy measurements with other measures of the emissivity density—e.g, from deep sub-millimeter surveys followed up by redshift determinations—to determine the bias of the sources.

Other important sources of fluctuation power over the relevant range of frequencies and angular scales are the cosmic microwave background (CMB), the shot noise due to the discrete nature of the FIRB sources, and thermal emission from dust in our own Galaxy. The CMB prevents measurements of the FIRB at frequencies less than about 200 GHz. Even at 200 GHz the angular power spectrum of the CMB is over an order of magnitude larger than the FIRB's, but with a sufficiently sensitive lower frequency CMB map one could use the well-known spectral depen-

¹Hubble Fellow

dence of the CMB to subtract it with high precision. We expect the correlated FIRB fluctuations to dominate the shot-noise contribution at multipole moments $\ell \lesssim 1500$, or angular scales $\gtrsim 7'$. Thermal emission from dust in our own galaxy could easily be confused with FIRB anisotropy, but, as we show below, the dust fluctuation power has a strong spatial dependence. There are regions of sufficiently low dust fluctuation power that the FIRB fluctuations are dominant at $\ell \gtrsim 60$ (angular scales $\lesssim 3^\circ$) at low frequencies. This critical multipole moment slowly increases as the frequency increases towards $\nu \sim 1000$ GHz and then rapidly increases beyond there, as the Milky Way dust appears hotter than the high- z dust contributing to the FIRB. Between these frequency and multipole moment limits, the FIRB correlations can be studied without the need for aggressive foreground subtraction.

Our work has been largely motivated by the proposed balloon-borne Explorer of Diffuse Galactic Emissions² (*EDGE*), which will survey the sky in 10 frequency bands from 150 GHz to 1290 GHz, with angular resolution ranging from $14'$ to $6'$ full-width half-maximum (FWHM). Later in the decade, the *Planck* surveyor³ should provide high-quality maps of correlated FIRB anisotropy at 217, 320, 545 and 850 GHz. We forecast the errors on the scale- and redshift-dependent product of bias and emissivity that could be reconstructed from *EDGE* and *Planck* observations. We also discuss how these quantities could be disentangled from uncertainties in the cosmological model and the emission spectrum of the sources.

Both sets of observations can reconstruct the product of emissivity and bias to $\sim 10\%$ in 4 redshift bins with the highest one extending from $z = 2$ to $z = 4$. Indeed, the constraints are $\sim 1\%$ if one considers smoother models for the bias-weighted emissivity. This level of precision is hard to duplicate by directly observing the clustering properties of the sources. It may be possible to resolve the background as a function of redshift in several frequency bands in the next decade using, e.g., BOLOCAM (Glenn et al. 1998) on the Large Millimeter Telescope (LMT) or the Atacama Large Millimeter Array⁴ (ALMA) and doing follow-up optical redshift determinations. However, we show that determining the clustering of the sources to $\lesssim 10\%$ accuracy at large enough scales to be in the linear regime requires many thousands of sources with follow-up redshifts of very faint galaxies.

Other missions may also detect the correlated FIRB anisotropy. The TopHat experiment⁵, with its 660 GHz channel, may provide an early opportunity for studying the FIRB anisotropy. The balloon-borne Bolometric Large Aperture Sub-millimeter Telescope⁶ (*BLAST*), designed to detect sources at the bright and rare end of the source count distribution, may also be able to measure fluctuations in the diffuse background.

Indeed, detectable FIRB correlations may even be lurking in existing data sets. Using the ISOPHOT instrument on ISO⁷, the shot noise of the FIRB has been seen

at $170\mu\text{m}$ (1760 GHz) but the galactic dust emission, at least in the field observed, has obscured the FIRB correlations (Lagache & Puget 2000). The correlations may be detected upon further analysis of the ISO data (after some dust cleaning), or in the *BOOMERanG* 420 GHz data (de Bernardis et al. 1999), or even possibly in the *COBE*/FIRAS data. Kashlinsky & Odenwald (2000) claim a tentative detection of correlated fluctuations in the *near*-infrared background using *COBE*/DIRBE data shortward of $10\mu\text{m}$, with somewhat greater amplitude than that predicted by Jimenez & Kashlinsky (1997).

The remainder of our paper is organized as follows. In § 2, we review what is known about the sources of the FIRB and about the mean spectrum. In § 3, we describe both the correlated and shot-noise contributions to the anisotropy. For the correlated component we demonstrate the dependence of the angular power spectrum on the fluctuation power in the FIR emission at different redshifts. In § 4, we describe the fluctuation power in the sky at the frequencies of interest from the other relevant components: thermal emission from dust in our own Galaxy, the CMB, and the FIRB. In particular, we emphasize the wide distribution in amplitudes of dust power spectrum across the sky. In § 5, we discuss qualitatively the reconstruction of various interesting physical quantities from FIRB observations, and then forecast *EDGE* and *Planck* errors on a reconstruction of a scale- and redshift-dependent product of bias times emissivity. We discuss our results in § 6, with an emphasis on the complementary nature of point source observations, and summarize our conclusions in § 7.

Although we maintain generality in all derivations, we illustrate our results with the currently favored ΛCDM cosmological model. Our choices for cosmological parameters are $\Omega_c = 0.30$, $\Omega_b = 0.05$, $\Omega_\Lambda = 0.65$, $h = 0.65$, $n = 1$, and *COBE* normalization of $\delta_H = 4.2 \times 10^{-5}$ (Bunn & White 1997). We use the fitting formula for the transfer function given by Eisenstein & Hu (1999). This model has mass fluctuations on the $8h^{-1}$ Mpc scale in accord with the abundance of galaxy clusters $\sigma_8 = 0.86$ (Viana & Liddle 1999).

2. FIRB MEAN

In this section, we review what is known about the FIRB mean, both from the FIRAS determination of its spectrum and from observations of sources—most notably at $850\mu\text{m}$ by the Sub-millimetre Common User Bolometer Array (SCUBA) camera (Holland et al. 1998) on the James Clerk Maxwell Telescope (JCMT). We emphasize the connection, created by the redshifting of the peak of FIR emission, between studying the background spectrum at low frequencies and determining the FIR emissivity at high redshifts.

2.1. The Spectrum

A grey body with power-law emissivity has been fit to the spectrum of the mean FIRB as determined with the *COBE*/FIRAS data (Fixsen et al. 1998, hereafter F98):

$$I_\nu = \tau_0(\nu/\nu_0)^\alpha B_\nu(T) \quad (1)$$

where $B_\nu(T)$ is the Planck function and τ_0 is the optical depth at $\nu_0 = 3$ THz. F98 find $\tau_0 = (1.3 \pm 0.4) \times 10^{-5}$, $T = 18.5 \pm 1.2$ K and emissivity power-law index $\alpha = 0.64 \pm 0.12$; this spectrum is plotted in Figure 1.

²<http://topweb.gsfc.nasa.gov>

³<http://astro.estec.esa.nl/Planck/>; also, ESA D/SCI(6)3.

⁴<http://www.almajrao.edu>

⁵<http://topweb.gsfc.nasa.gov/>

⁶<http://www.hep.upenn.edu/blast/>

⁷see <http://isowww.estec.esa.nl/> for details

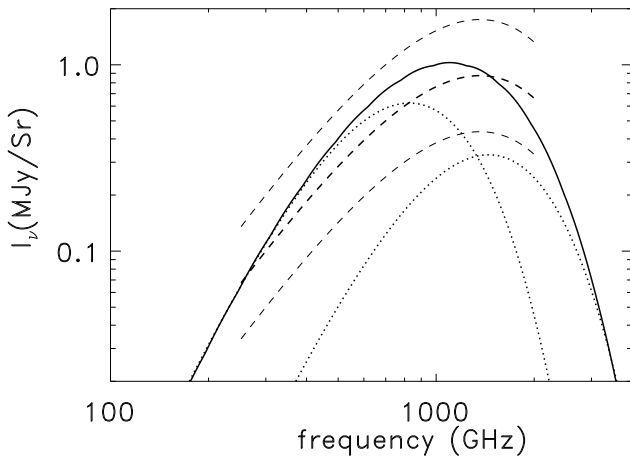


FIG. 1.— The spectrum of the FIRB predicted in the HK00 standard model (solid curve). The dashed curves show the measurements with $\pm 1\sigma$ uncertainties from F98. The light dotted curves are grey-body spectra with $\alpha = 2$ and $T = 8$ K (left curve) and $T = 14$ K (right curve). Their optical depths and temperatures are chosen to match the low frequency and high frequency sides of the HK00 spectrum. The HK00 spectrum is a sum of many such grey-body spectra.

HK00 considered a variety of models to describe the FIRB spectrum. For the present calculations, we use only the “standard model” from HK00, which we refer to simply as the HK00 model. Its spectrum is shown in Fig. 1, with the amplitude reduced by 40% relative to HK00 to be in better agreement with the FIRAS data. We apply the reduction throughout this paper, thereby reducing the angular power spectra by a factor of 2. The HK00 model for the FIRB mean assumes that the UV emissivity at each redshift is proportional to the star-formation rate (SFR) as estimated by Madau (1999), that dust production is proportional to the SFR, and that the dust has the optical properties of the Draine and Lee (1984) model. With the optical properties and radiation backgrounds specified, the dust temperature follows. The two proportionality constants for the UV emissivity and dust production are set to produce a spectrum that is consistent with the F98 determination.

On the Rayleigh–Jeans side of the spectrum, Draine and Lee (1984) dust is a grey body with emissivity index $\alpha = 2$. Thus the HK00 spectrum is a sum of such grey bodies with varying apparent temperatures and optical depths, where apparent temperature is defined as $T_{\text{app}} = T/(1+z)$ where T is the physical temperature. The HK00 spectrum cannot be fit by a single grey body with $\alpha = 2$. We demonstrate this in Fig. 1 with the $\alpha = 2$ grey bodies plotted as dotted curves. For the right-most dotted curve, we chose the temperature and optical depth to fit the curve at high frequencies. Moving towards lower frequencies, this $T_{\text{app}} = 14$ K grey body quickly falls below the HK00 spectrum. To fit the spectrum, one must add in colder components, such as the $T_{\text{app}} = 8$ K one shown. Clearly, in this particular model, there is not much need for even colder components. Since the HK00 model has dust with $T \approx 24$ K in the redshift range 1 to 4, this indicates that most of the FIRB in this model comes from $z < 2$. Note that the F98 fit to the FIRAS data is even softer than the

HK00 model, possibly due to the presence of even colder (higher redshift) components, although it should be kept in mind that the uncertainties in this slope at low frequencies are quite large.

In principle, one can take the spectrum of the background and, assuming the emissivity index, reconstruct the optical depth of each temperature component. This is the essence of the idea recently discussed and implemented by Gispert et al. (2000). By assuming the shape of the average SED, one can recover the FIR luminosity density as a function of redshift, which can be related to the SFR using certain assumptions.

Due to the large size of the FIRAS uncertainties, especially at frequencies less than ~ 300 GHz, this reconstruction can not be done accurately. Furthermore, there are no proposed missions for improving upon FIRAS’s determination of the FIRB spectrum, which we understand to be a very difficult task. Fortunately, one can make quite similar use of a measurement of the spectrum of the FIRB *anisotropy*—although with the added complication that one is not reconstructing the luminosity density, but the luminosity density weighted by the clustering bias of the sources. A differential measurement of the spectrum should be able to measure to lower frequencies due to the fact that the amplitude of the CMB anisotropy is about 10^{-5} of the CMB monopole. This is especially interesting since the limiting redshift (coldest component) one can reach is determined by the lower frequency limit of the spectrum determination. We turn to a description of the FIRB anisotropy in § 3.

2.2. Resolving the Background

The mean brightness of a background due to point sources depends on the number density of sources as a function of limiting flux, $N(>S)$:

$$I = \int (S^2 dN/dS) d\ln S. \quad (2)$$

Notice that the bulk of the background is contributed by sources near the maximum of $S^2 dN/dS$. We therefore show this function as predicted by the semi-analytic modeling of Guiderdoni et al. (1998, hereafter G98) at several frequencies in Fig. 2. G98 calculated predictions for a range of models; we use their model E predictions, which are the ones in best agreement with the observations available at $850\mu\text{m}$.

Considerable progress has been made towards resolving the FIRB into discrete point sources (Hughes et al. 1998; Barger et al. 1998; Eales et al. 1999; Smail et al. 1997; Holland et al. 1998; Blain et al. 1999b; Barger et al. 1999a; Puget et al. 1999; Barger et al. 1999b; Blain et al. 1999c). In particular, the SCUBA camera (Holland et al. 1998) on the JCMT has been used to identify point sources at $850\mu\text{m}$ that account for a large fraction, $\sim 50\%$, of the FIRB at these wavelengths (Barger et al. 1999a). As shown in Figure 2, the SCUBA detections are in the range of ~ 1 mJy to ~ 10 mJy, presumably near the peak of $S^2 dN/dS$. The result of fitting a double power-law form for $N(>S)$ to the SCUBA data, with the constraint that it reproduce the FIRAS-determined mean (Barger et al. 1999a), results in the light solid line in Figure 2.

Followup observations of SCUBA locations at radio, optical and infrared wavelengths have suggested possible

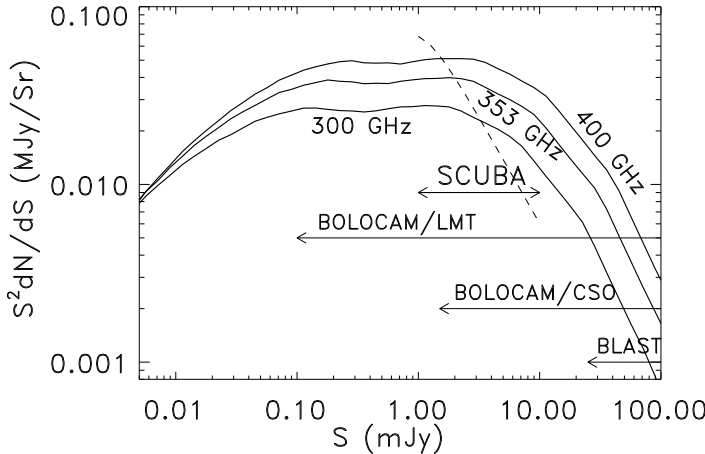


FIG. 2.— The contribution to the FIRB mean from each logarithmic interval in S , according to model E (G98) at 300 GHz, 353 GHz and 400 GHz. The light dashed line is a fit to the SCUBA data, which covers the ~ 1 mJy to ~ 10 mJy range (Barger et al. 1999a). Future observations near these frequency ranges will go deeper and broader. The left-hand limits for BOLOCAM, observing at 270 GHz, are the 5σ sensitivities after a 10-hour pointing at a single field-of-view. Both of these pointing should result in the detection of about 60 sources according to model E (G98). The left-hand limit for BLAST is the 5σ limit for the deepest of their planned surveys, which takes 2 days of a 10-day long-duration balloon flight. The vertical location of the indicated survey ranges is arbitrary.

counterparts, albeit with a relatively low identification rate. Typical sources are identified as galaxies with moderate to massive star formation rates. Optical redshifts, the sub-millimeter to radio spectral index (e.g. Carilli & Yun 1999) and the detection of CO molecular lines (Frayer et al. 1999) suggest that most of these sources lie at redshifts ranging from 1 to 4. For a recent review of SCUBA results see Smail et al. (2000). Continued followup observations of SCUBA surveys and those that were carried out with ISO, such as the European Large Area ISO Survey (Efstathiou et al. 2000; Serjeant et al. 2000; Oliver et al. 2000), will provide important details on the physical properties of far-infrared (FIR) emission and the redshifts of contributing sources.

Further progress towards resolving the background in wave bands near $850\mu\text{m}$ (353 GHz) will come soon from a bolometer array sensitive to $1100\mu\text{m}$ (273 GHz) called BOLOCAM, now at the Caltech Submm Observatory (CSO). When deployed on the LMT, it will have sufficient resolution to resolve considerably more of the background. *BLAST* will be able to detect the brightest sources at $750\mu\text{m}$ (400 GHz) and also has detectors at 300 and $200\mu\text{m}$, to permit the determination of color redshifts. The California Millimeter Array (CARMA), an interferometer composed of existing BIMA and Owens Valley telescopes, is expected to carry out observations at 235 and 345 GHz with \sim arc second resolution that will allow cross-identification at optical wavelengths, allowing further followup observations (Carlstrom 2000). Finally, ALMA will have high sensitivity and very high angular resolution. In a single 10 hour pointing, it will achieve a 5σ noise level of 0.03 mJy and still be far from the confusion limit. However, many such pointings will be required to get large numbers of sources, as the field-of-view is only 0.07 square

arcminutes, over which model E predicts about six sources brighter than 0.03 mJy.

At shorter far-infrared wavelengths, a smaller fraction of the background has been resolved. For example, the FIRBACK survey at $170\mu\text{m}$ with ISOPHOT on ISO (Puget et al. 1999) has resolved about 10% of the background (Puget et al. 1999). Much progress will come in the near future from MIPS on *SIRTF* (160, 70 and $24\mu\text{m}$), SPIRE and PACS on *FIRST* (90 to $500\mu\text{m}$), and HAWC on *SOFIA* (60, 110 and $200\mu\text{m}$). Information on most of these sub-millimeter and far-infrared instruments is summarized in Blain (1999d).

3. FIRB ANISOTROPY

The FIRB is anisotropic at small scales due to the discrete nature of the sources, and at larger scales due to correlations between these sources. We first discuss the correlated anisotropy.

3.1. FIRB correlations

The antenna temperature of the FIRB at a given frequency ν and in a given direction $\hat{\mathbf{n}}$ can be written as a line of sight integral of the product between the mean FIR emissivity and its fluctuation:

$$T(\hat{\mathbf{n}}, \nu) = \int dz \frac{dr}{dz} a(z) \bar{j}(\nu, z) \left[1 + \frac{\delta j(r(z)\hat{\mathbf{n}}, \nu, z)}{\bar{j}(\nu, z)} \right], \quad (3)$$

where r is the coordinate distance (or conformal time) from our location at the coordinate origin and $\bar{j}(\nu, z)$ is the mean emissivity per comoving unit volume at frequency ν as a function of redshift z . In a flat universe, which we will assume, r is simply the proper motion distance. We will always use comoving wavenumbers and spatial scales.

We next wish to derive the angular power spectrum $C_\ell^{\nu\nu'}$ of the FIRB, which is the Legendre transform of the two-point correlation function

$$C(\hat{\mathbf{n}}, \hat{\mathbf{m}}) \equiv \langle T(\hat{\mathbf{n}}, \nu) T(\hat{\mathbf{m}}, \nu') \rangle = \sum_l \frac{2l+1}{4\pi} C_l^{\nu\nu'} P_l(\hat{\mathbf{n}} \cdot \hat{\mathbf{m}}). \quad (4)$$

This is most easily done by first decomposing the temperature maps into spherical harmonic multipole moments,

$$a_{lm}(\nu) = \int d\hat{\mathbf{n}} T(\hat{\mathbf{n}}, \nu) Y_l^{m*}(\hat{\mathbf{n}}). \quad (5)$$

With an isotropic random field, the second moments of these multipole coefficients are

$$\langle a_{l_1 m_1}^*(\nu) a_{l_2 m_2}(\nu') \rangle = \delta_{l_1 l_2}^D \delta_{m_1 m_2}^D C_l^{\nu\nu'}. \quad (6)$$

Using equation (3), we can rewrite equation (5) as

$$a_{lm}^{\text{FIRB}}(\nu) = \int d\hat{\mathbf{n}} Y_l^{m*}(\hat{\mathbf{n}}) T(\hat{\mathbf{n}}, \nu) = i^l \int \frac{d^3 \mathbf{k}}{2\pi^2} \delta(\mathbf{k}) I_l^{\text{FIRB}}(k, \nu) Y_l^{m*}(\hat{\mathbf{k}}), \quad (7)$$

where

$$\begin{aligned} I_l^{\text{FIRB}}(k, \nu) &= \int dz \frac{dr}{dz} W^{\text{FIRB}}(k, \nu, z) j_l(kr) \\ &\approx W^{\text{FIRB}}(k, \nu, z) \int dz \frac{dr}{dz} j_l(kr) \\ &= W^{\text{FIRB}}(k, \nu, z) \frac{\sqrt{\pi} \Gamma[(l+1)/2]}{2k \Gamma[(l+2)/2]}, \end{aligned} \quad (8)$$

and

$$W^{\text{FIRB}}(k, \nu, z) = a(z)G(z)\bar{j}(\nu, z)b(k, \nu, z). \quad (9)$$

Here, $G(z)$ is the linear theory growth function (Peebles 1980), j_ℓ is the usual Bessel function, and the approximation used follows the well-known Limber form (Limber 1953). The ratio of Gamma functions goes to $\sqrt{2/\ell}$ for $\ell \gg 1$.

In equation (7), $\delta(\mathbf{k})$ is the linear theory dark matter density fluctuation today, $\delta \equiv \delta\rho/\bar{\rho}$. It enters because we have assumed, as in HK00, that the fluctuations in the emissivity, $\delta j/\bar{j}$, are a biased tracer of those in the mass. In general, this bias can depend on scale, frequency, and redshift, so that in Fourier space we write:

$$\frac{\delta j(\mathbf{k}, \nu, z)}{\bar{j}(\nu, z)} = b(k, \nu, z)\delta(\mathbf{k}, z). \quad (10)$$

We ignore the possibility of stochastic bias (Dekel & Lahav 1999) until the discussion.

With these assumptions about the bias we can finally write the angular power spectrum of FIRB anisotropy using the three-dimensional, linear-theory power spectrum of dark matter density fluctuations today, $P_M(k)$,

$$\langle \delta(\mathbf{k}, z)\delta^*(\mathbf{k}', z) \rangle = (2\pi)^3 \delta^D(\mathbf{k} - \mathbf{k}') P_M(k) G^2(z), \quad (11)$$

as a line of sight projection

$$C_l^{\nu\nu'} = \int \frac{dz}{r^2} \frac{dr}{dz} a^2(z) j_b(k, \nu, z) j_b(k, \nu', z) P_M(k) \Big|_{k=\frac{l}{r}} G^2(z) \quad (12)$$

We have used the Limber approximation which sets $k = l/r$. At $\ell = 30$ the Limber approximation is valid here to within 10% of the exact (first order) calculation and rapidly converges to the exact value as ℓ increases. Since the bias factor enters into the expression for $C_l^{\nu\nu'}$ multiplied by the mean emissivity, we define the “bias-weighted emissivity” j_b as

$$j_b(k, \nu, z) \equiv b(k, \nu, z)\bar{j}(\nu, z). \quad (13)$$

We do not use the above equations in their full generality. We follow HK00 in assuming that the bias is a constant, i.e., independent of frequency, redshift and scale. We take this bias to be 3, which will roughly match the observations of the clustering of $z = 3$ Lyman-break galaxies (Steidel et al. 1998; Giavalisco et al. 1998; Adelberger et al. 1998). Bias is likely to increase with redshift (Baugh et al. 1999; Blanton et al. 2000), and hence this approximation may down-weigh the relative importance of fluctuation power at high redshift. The bias may also be frequency dependent, which could result from two different populations of sources, each with different spectral energy distributions and clustering properties. We briefly discuss such a possibility below but neglect it for now in order to illustrate the nature of the observables in the simplest possible case.

We wish to understand how measurements of $C_l^{\nu\nu'}$ can be used to determine the bias-weighted emissivity j_b as a function of redshift. To that end we display contributions to the angular power spectra from various redshift ranges in Figure 3. As stated above, we have assumed that the bias is redshift-independent and that the mean emissivity is that of the HK00 standard model.

Figure 3 shows that the relative contributions from the various redshift ranges depends on the observed frequency

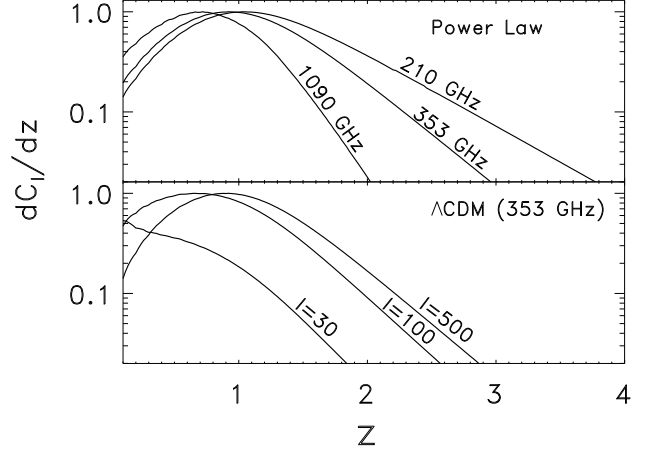


FIG. 3.— $dC_l^{\nu\nu'}/d\nu$ for a power-law 3D power spectrum (solid lines) at, from right to left, $\nu = 210, 353$ and 1090 GHz, all normalized to unity at their maximum. For any power-law 3D power spectrum, these are independent of ℓ . The three curves in the bottom panel show the same quantity, using a Λ CDM power spectrum at 353 GHz, for $\ell = 30, 100$, and 500 respectively.

and on the shape of the matter power spectrum. In the top panel, we consider a power-law power spectrum, $P(k) \propto k^{-2}$, and show the shape of the redshift breakdown $dC_l^{\nu\nu'}/dz$ for three frequencies, $\nu = 210, 353$ and 1090 GHz. These are the integrands of equation (12). Note that lower frequencies probe to higher redshifts, as expected. For any power-law power spectrum, the shape of $dC_l^{\nu\nu'}/dz$ as a function of z is the same for all values of ℓ .

The non-power-law nature of physical power spectra lead to different shapes of $dC_l^{\nu\nu'}/dz$ for different values of ℓ . In the lower panel of Figure 3, we plot three different ℓ at fixed frequency for the Λ CDM model. Higher ℓ map to smaller scales, where the spectral index of the power spectrum is more negative. This means that higher redshifts, where the spatial scale corresponding to a given ℓ is larger, contribute more to the anisotropies. Hence, higher ℓ probe higher redshifts.

Figure 4 shows the contributions to $C_l^{\nu\nu'}$ for different redshift ranges and frequencies. In each panel, one can see the shape dependence of the contribution from each redshift interval, with lower redshifts having more low- ℓ fluctuation power compared to the high-redshift intervals. This shape dependence aids in the reconstruction of the redshift dependence of the fluctuation power. Comparing the panels, one should note the more rapid drop-off towards higher redshift at 850 GHz than at 210 GHz. At the higher frequency, there is very little contribution from $z \gtrsim 1.5$.

We now turn to the cross-frequency correlations. In Figure 5, we show the expected cross-correlations between measurements at 390 GHz and those at four other frequencies ($210, 852, 1060$, and 1290 GHz). The lowest frequencies are affected by all the redshifts that have any significant fluctuation power; therefore, these frequencies weight all of the fluctuations in the same way and are therefore highly correlated. Higher frequencies are insensitive to high-redshift fluctuations because they fall on the Wien side of the redshifted spectrum. With only a por-

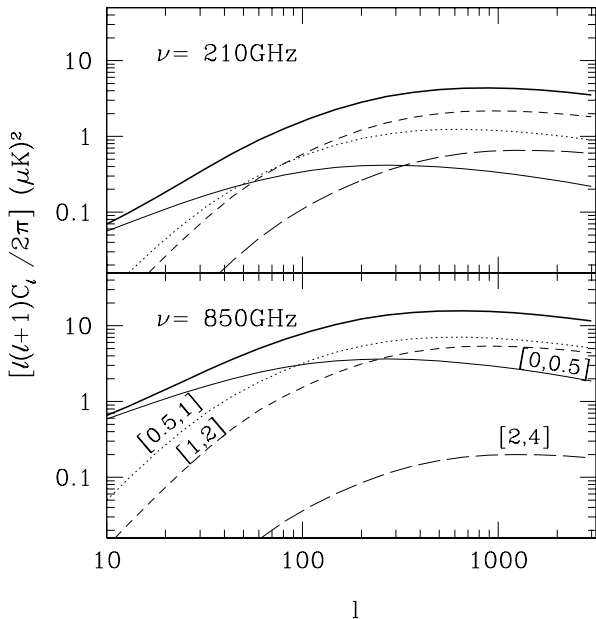


FIG. 4.— Contributions to $C_l^{\nu\nu}$ from several redshift ranges (labeled in lower panel) for $\nu = 210$ GHz (upper panel) and $\nu = 850$ GHz (lower panel). The heavy solid line is the total power spectrum observed at $z = 0$.

tion of the fluctuations included, the degree of correlation degrades. The break frequency, at which this correlation departs from unity, is sensitive to the onset of significant fluctuation power in FIR galaxies. Because higher ℓ 's are preferentially more sensitive to higher z , the diminishing importance of high- z at higher frequencies is more pronounced at smaller angular scale.

It is important to keep in mind that the redshift-dependences of the power spectra, illustrated in figures 3 and 4, and the cross-correlations shown in figure 5 are those of a particular model—the HK00 standard model. For this model the emissivity tracks the star formation rate as determined by Madau et al. (1998), which is quite uncertain. It is possible that the SFR is much higher at high-redshift. If one assumes efficient conversion of gas into stars in all collapsed halos down to some small mass (with virial temperatures of about 10^4 K) then there is a peak in the SFR at $z \sim 7$ (e.g. Haiman et al. 2000) which is seen in simulations (Gnedin & Ostriker 1996). Increased high- z SFR would lead to a greater fraction of the fluctuation power coming from high redshifts, and greater decorrelation between the high and low frequencies.

We use the linear-theory evolution of the matter power spectrum in our calculations. At $z \approx 1$, the non-linear corrections become important at wavenumbers $k \gtrsim 0.4h \text{ Mpc}^{-1}$, which projects to $\ell \gtrsim 800$. At lower redshifts, this non-linear scale moves to smaller ℓ , but the FIRB contributions drop as well (see the higher ℓ curve in Fig. 3). At $\ell \approx 1000$, non-linear corrections produce a 20% increase in the FIRB angular power spectrum. Because this is a small difference that can be accurately included for any chosen cosmology, neglecting the non-linearity won't affect our quantitative results. However, we do restrict our analysis to $\ell < 1600$ both to avoid the deeply non-linear

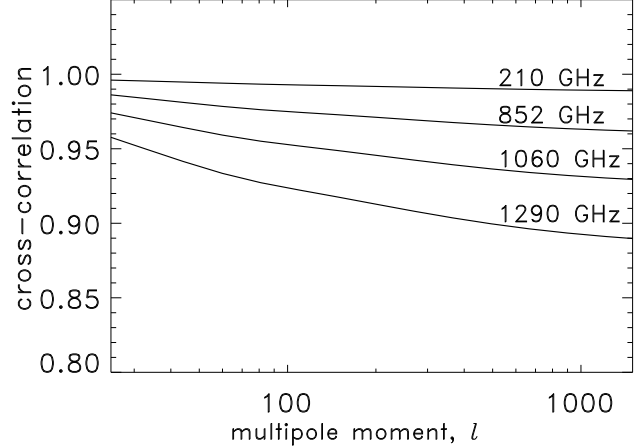


FIG. 5.— Cross-correlations $C_l^{\nu\nu'} / \sqrt{C_l^{\nu\nu} C_l^{\nu'\nu'}}$ vs. ℓ between the $\nu = 390$ GHz channel and four other frequencies $\nu' = 210, 852, 1060$, and 1290 GHz.

regime and to eliminate the need for detailed shot noise subtraction.

3.2. Shot Noise

At smaller angular scales, the fact that the FIRB comes from individual, well-separated sources introduces anisotropy simply due to the Poisson sampling of the density field. This so-called shot noise can be calculated from the source counts by

$$C_i^{\text{shot}} = \int (S^3 dN/dS) d \ln S. \quad (14)$$

Note that this is more heavily weighted towards the bright end of the distribution than the mean brightness was (eq. [2]).

For a Euclidean distribution (appropriate for galaxies at low redshift), $dN/dS \propto S^{-2.5}$ and so the integrand diverges at the bright end. However, in the case of the FIRB (at least as modeled by G98 model E), the enormous number of faint, high-redshift sources cause the source counts to become steeper than $S^{-2.5}$ at fainter flux levels. Even if we remove sources only down to the very conservative flux level S_{cut} such that $N(>S_{\text{cut}}) = 1$ per 4π steradians, the FIRB shot noise is still dominated by the fainter, high-redshift population. Therefore, we take our shot noise estimates from the G98 model E counts, assuming only a cut at one source per sky and avoid any complications of source removal. The number of sources detected at greater than 5σ by *EDGE*, according to model E, are given in Table 1. The removal of these sources from the map does not significantly reduce the shot noise.

4. FOREGROUNDS AND BACKGROUNDS

There are celestial sources of emission in the far infrared and sub-millimeter other than the FIRB. To detect the correlations of the high-redshift galaxies that make up the FIRB, we need to be able to separate this signal from all the other sources. The two most important contributions come from the CMB anisotropies and thermal emission from dust in our own Galaxy. Radio foregrounds such as synchrotron, Bremsstrahlung, and rotational emission

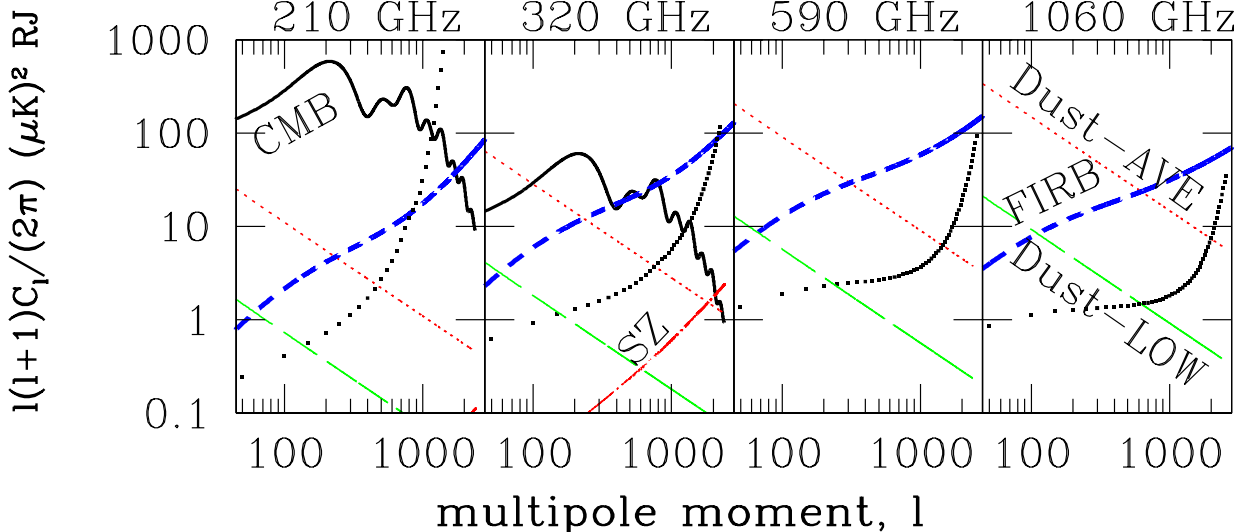


FIG. 6.— Power spectra of the dominant components of the far infrared sky at four different frequencies measured by *EDGE*. All are labeled in at least one of the panels. The thick solid curves show the CMB in a flat Λ CDM model; the thick dashed curves show the FIRB predictions for the HK00 model including contributions from nonlinear evolution and from shot noise as predicted by model E (G98); the thin dotted and long dashed curves show the dust spectrum representing an average over the cleanest 50% of the sky, as well as a spectrum of the cleanest regions, respectively; and the thick (square) dotted curves with spacings of $\delta l = 50$ are errors expected on the determination of the FIRB power spectrum from a 10-day flight of *EDGE*.

from dust do not appear to be significant at $\nu \gtrsim 200$ GHz. Reviews of what is known about galactic dust emission and other CMB foregrounds can be found in de Oliveira-Costa & Tegmark (1999).

Figure 6 shows the predicted power spectra of the components at 4 different *EDGE* frequencies. The FIRB angular power spectrum is shown by the thick dashed curves for the standard, constant bias model of HK00. Unlike in all previous figures in this paper, these curves include a shot-noise contribution, computed from the G98 model E, as well as the effects of the non-linear evolution of the matter power spectrum. Other lines show the contributions of the CMB and Galactic dust, which we will now discuss in detail.

4.1. CMB

The thick solid curves in Figure 6 show the CMB power spectrum in our flat Λ CDM model, consistent with the *COBE/DMR*, *Boomerang* and *Maxima* measurements (de Bernardis et al. 2000; Hanany et al. 2000; Jaffe et al. 2000). As one can see from this figure, the CMB anisotropies are the dominant source of fluctuation power on the sky over a substantial range of ℓ at low frequencies. The FIRB anisotropies would be swamped by such a signal. Fortunately, the spectrum of the CMB anisotropies is well-known, so that one can use observations at yet lower frequencies (where the contrast between the CMB and the FIRB is even starker) to clean the CMB signal out of the FIRB maps.

To demonstrate the ability of a particular experiment to subtract the CMB, we have forecasted errors on the determination of the FIRB power spectrum for 4 of the *EDGE* channels. The results, in bins of $\delta l = 50$, are plotted in Fig. 6. For each of the error forecasts at 210, 320, 590 and 1060 GHz, we use only two channels—the channel

in question plus the 150 GHz channel (as a CMB monitor). Note that the 590 and 1060 GHz channels require no CMB cleaning, and therefore the FIRB measurement is sample-variance limited until the beam becomes important at $\ell > 1000$. At 210 and 320 GHz, the errors increase above sample variance at much lower ℓ , due to imprecise cleaning of the CMB. Even at these low frequencies, the CMB can be subtracted sufficiently accurately to allow for $\delta C_l/C_l < 1$ in bins of $\delta l = 50$ up to $\ell \sim 1000$. The more sensitive and higher angular resolution 100 GHz channel on *Planck* allows for even better CMB subtraction. More details on these power spectrum error forecasts are given in section 5.2. For now, we simply state that our calculations include the errors that result from the detector noise, sample variance, and the cleaning of CMB using the 150 GHz channel of *EDGE*. They do not include the effects of contamination by interstellar dust, which we discuss next.

4.2. Dust

Galactic dust is far from being an isotropic Gaussian random field and is a more dangerous contaminant because its frequency dependence is more uncertain and varies spatially. Moreover, dust can contribute significantly to the signal over the entire frequency range where we have a hope of measuring the FIRB. A very encouraging point, however, is that the amplitude of the dust power spectrum varies considerably over the sky. In particular, as we will demonstrate, there are a number of sizeable fields with substantially less fluctuation power than average, even when that average is restricted to high galactic latitude. Hence, an important part of any plan to observe FIRB fluctuations is to choose fields with very low dust fluctuation power.

We begin from the millimeter-wave predictions of the two-component dust model of Finkbeiner et al. (1999,

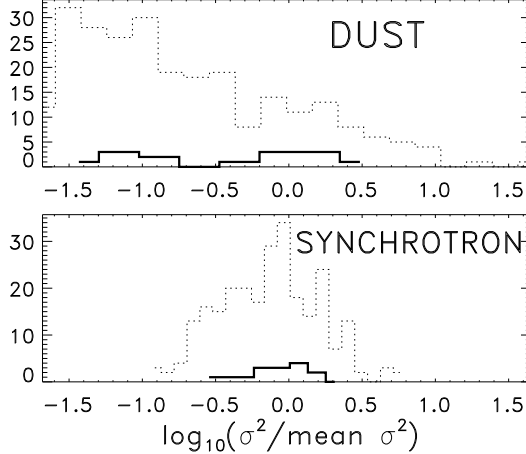


FIG. 7.— Histograms of variance in units of the mean variance for square patches in an $80^\circ \times 80^\circ$ field centered on the SGP. Light dotted lines are for the 256 patches, each $5^\circ \times 5^\circ$, and the heavy solid lines are for the 16 patches, each $20^\circ \times 20^\circ$. The top panel is for dust emission at 300 GHz, and the bottom panel is for synchrotron emission at 30 GHz. Dust maps are the predictions at 300 GHz (Finkbeiner et al. 1999). The mean dust variances are $(9.8 \mu\text{K})^2$ (small patches) and $(15 \mu\text{K})^2$ (large patches). Synchrotron maps are WOMBAT predictions at 30 GHz. The mean synchrotron variances are $(22 \mu\text{K})^2$ (small patches) and $(40 \mu\text{K})^2$ (large patches).

hereafter F99). The two-component model has two direction-dependent parameters which are fixed by Diffuse Infrared Background Explorer (DIRBE) and Infrared Astronomy Satellite (*IRAS*) measurements at 100 and 240 μm . The optical properties of the dust are assumed to be spatially uniform and were chosen to give the best possible agreement with the *COBE*/FIRAS data at longer wavelengths. Software for making full-sky predictions of this model combined with the *COBE*/DIRBE and *IRAS* data is available from the Wavelength-Oriented Microwave Background Anisotropy Team⁸ (WOMBAT).

We select an $80^\circ \times 80^\circ$ field centered on the south Galactic pole (SGP) and calculate the power spectrum at *EDGE* frequency bands in sixteen $20^\circ \times 20^\circ$ sub-fields. All sub-fields had power spectra C_ℓ roughly proportional to $1/\ell^3$ (as found by, e.g., Gautier et al. (1992); Wright (1998)). The histogram of the variances of these sub-fields is shown in Figure 7. The differences between the fields is very large. While the SGP as a whole is separated from the worst of the Galaxy's dust emission, 4 of the 16 sub-fields have a variance less than 1/16 of the average SGP sub-field variance.

In Figure 6, the “Dust–AVE” lines at each frequency are normalized to have a variance equal to the mean variance of the SGP field as a whole, whereas the “Dust–LOW” curves have a variance 1/16 smaller. The cleaner sub-fields have such low dust emission that the FIRB fluctuations should completely dominate. In light of this, for the purposes of forecasting FIRB parameter errors in § 5, we have allowed ourselves to treat the dust in a very simple manner. We assume that the dust emits a grey-body spectrum with emissivity index $\alpha = 2$ and a temperature of 18°K , completely coherent between frequency bands, with an angular power spectrum falling as $C_\ell \propto l^{-3}$. The amplitude

is the same as the “Dust–LOW” curves at 320 GHz. This single-component model, normalized at 320 GHz, is sufficient for our purposes in forecasting results from *EDGE*. In the low-dust regions, the dust is sufficiently unimportant that our results are insensitive to the details of the modeling. To fully understand what can be learned from full-sky surveys, such as *Planck*, we would need a more sophisticated modeling of the dust. Here, we simply assume that the “Dust–LOW” amplitudes apply to *Planck* as well but include only 10% of the sky.

In Figure 6, we also show the results of repeating the sub-division of the SGP into 256 sub-fields, each $5^\circ \times 5^\circ$. The smaller patches show even greater variation in the dust fluctuation power. Thus, for deep small-field observations, one can lower the dust contamination greatly by choosing the right fields to observe. This may be particularly important for attempts to measure the polarization of the CMB.

Finally, for comparison, we have done the same exercise with WOMBAT predictions for 30 GHz synchrotron maps. These show significant variation, but much less than the dust, presumably due to the larger galactic scale-height for synchrotron emission.

5. FORECASTED PARAMETER ERRORS

With the formalism in place and the physical components specified, we can now proceed to consider how measurements of the FIRB anisotropies constrain the emissivity, bias, and spectral energy distributions (SEDs) of the far-infrared sources as a function of redshift. However, we will first describe the degeneracy structure of the theory, so that the reader can better understand what combinations can be constrained and how our quantitative investigation should proceed.

5.1. Degeneracies and Reconstruction

Two major degeneracies affect the interpretation of FIRB anisotropies. First, changes in the emissivity of the sources may be compensated by changes in their bias (HK00), as evident in equation (12). Only the product j_b (eq. [13]) can be constrained by confusion-limited anisotropy measurements, and so we will work only with this quantity. Of course, the emissivity of the sources can be measured through the FIRB mean (§2) or through the study of sources from higher-resolution observations. Any separation of bias and emissivity from anisotropy measurements will require such external information.

Second, within confusion-limited observations, changes in the bias-weighted emissivity are partially degenerate with changes in the spectra of the sources coupled with a shift in redshift. Pedagogically, this degeneracy may be best understood by first considering the special case of a power-law matter power spectrum, for which the degeneracy is complete.

Imagine that each redshift emits a featureless spectrum with a high-frequency cutoff (e.g. a grey-body at some temperature). Each redshift will contribute anisotropy only to observed frequencies below the redshifted cutoff. As one considers higher frequencies, the contributions from different redshifts begin to drop out, starting with the highest redshifts. By measuring the reduction in anisotropy as well as the imperfect cross-correlation, one can

⁸<http://astron.berkeley.edu/wombat/>

isolate the contribution of the sources with that apparent cutoff frequency. If one knows the rest-frame frequency of the cutoff, then one can infer the redshift and use that redshift to map the angular power of the emission to its spatial power. By dividing the spatial power spectrum of the light by that of the mass, one finds the bias-weighted emissivity of the sources at each redshift.

However, if the emitted temperature is unknown, one cannot assign a redshift to a particular observed cutoff. For example, an increase in temperature of the emission would imply a larger redshift. This shift in redshift alters the mapping between physical and angular scale; however, because the spatial power spectrum is a power-law, the shift in distance scale can be compensated by a shift in normalization so as to leave the observed angular power spectrum unchanged. We thus have a degeneracy between the emitted spectrum, the redshift, and the bias-weighted emissivity of the sources. In models of interest, a 10% shift in $1+z$ mimics a 30% shift in fluctuation amplitude (60% in power).

Another way to describe this is to view the FIRB anisotropies as a sum of correlations of different *apparent* temperature components. By analyzing the frequency structure of the correlations, one can determine the power spectrum associated with each apparent temperature. However, unless one knows the original emitted temperature, one cannot determine the redshifts of the apparent temperature components. Without the redshift, one cannot convert the angular power spectrum to a spatial one.

The degeneracy is lifted when the power spectrum is not a power-law. With a feature or bend in the spatial power spectrum, one has a second handle on the redshift of the sources through the measurement of where the feature appears in angle. By combining the details of the frequency covariance with the location of features in the angular power spectrum, one can measure the emission spectrum separately from the bias and luminosity. Unfortunately, because CDM power spectra are fairly smooth and lack strong features, the redshift-temperature degeneracy is only partially lifted. The slow dependence of the comoving angular diameter distance on redshift further limits one's ability to measure the redshift.

The above paragraph assumed that the bias of the sources was scale-independent, so that scales in the matter power spectrum would shine through in the FIRB anisotropies. The bias may instead be scale-dependent. Even a smooth dependence on scale can shift the location of soft bends in the power spectrum, such as are found in CDM models. This would confuse the interpretation of the angular power spectrum in terms of redshift and skew the inferred bias-weighted emissivities. Of course, a general scale-dependent bias will ruin any use of the angular power spectrum to measure the redshift of the sources.

Because of the above concerns, we anticipate that the emission temperature and hence redshift of the sources will not be well-constrained by the FIRB anisotropies alone. In §5.2, we find that biases could be constrained in 4 redshift bins at the level of 5–15% if the emission spectra were known, but the large-angle FIRB anisotropies themselves will not deliver the $\sim 5\%$ emission temperature constraint that would be needed to break the degeneracy to this level. Instead, one must rely on external informa-

tion, notably from high-resolution infrared imaging with followup spectroscopy, to supply the emission spectrum as a function of redshift. Clearly, the spectral energy distribution of bright sources will be a good start. We caution only that the FIRB anisotropies actually require the bias- and luminosity-weighted spectral energy distribution of the sources. If the spectra of sources depends strongly on luminosity, it may be necessary to extrapolate to unresolved flux levels when integrating over the luminosity function.

Having noted this degeneracy, it is important not to over-react to it. First, allowing for uncertainty in the emission spectra will make the bias-weighted emission j_b uncertain, but there will be a combination of these parameters that will be well-constrained. Indeed, as shown in Appendix A of Eisenstein et al. (1999), the errors on the product of j_b and a calculable function of the spectral variation will be the same as the errors on j_b in the limit that the spectra are held fixed. In our quantitative work, we want to focus on this well-constrained combination of parameters; in breaking the degeneracy by fiat, we can calculate the errors on this quantity. We will show in §5.2 that the FIRB anisotropies can deliver several better than 10% constraints on the properties of FIRB sources.

Second, the emission temperatures in plausible models do not vary by large amounts. If the FIRB anisotropies were to reveal a factor of 8 change in emission as a function of redshift, it would be unrealistic to explain it by a factor of two shift in the temperature scale. While such coarse statements “waste” the precision of the FIRB anisotropy measurement, they do show that the measurements can yield interesting results without detailed external constraints on the emission properties.

In the same spirit, we will assume that the underlying cosmology is well known. Introducing uncertainties in that sector would cause additional degeneracies. Some are simple: the amplitude, shape, or time dependence of the matter power spectrum will be directly degenerate with the bias. Uncertainties in the relations between distance, volume, and redshift will cause more subtle problems akin to those described above. However, one can always map the constraints on j_b into constraints on a product of the j_b and functions of cosmology.

5.2. A Quantitative Study

For a quantitative assessment of what we can learn about $j_b(k, \nu, z)$ from measurement of $C_l^{\nu\nu'}$, we split j_b into four redshift bins with intervals of $[0, 0.5]$, $[0.5, 1]$, $[1, 2]$ and $[2, 4]$. We then parameterize j_b as follows:

$$j_b(k, \nu, z) = \sum_i \chi_{i(z)} \alpha_i j_b^s(k, \nu, z) (k/k_*)^{n_i} \quad (15)$$

where $\chi_{i(z)}$ is unity for z in the i^{th} redshift bin and zero otherwise. The parameters α_i and n_i adjust the amplitude and scale-dependence, respectively, of the bias-weighted emissivity in the i^{th} redshift bin. $j_b^s(k, \nu, z)$ is simply the j_b of the HK00 model (and actually has no k dependence). The pivot point k_* is chosen to project to $\ell = 500$ at all redshifts. As we will see, this is nearly the “sweet spot” at which the errors on α_i and n_i become independent. In total, the model has 8 free parameters: 4 amplitudes and 4 tilts.

TABLE 1

EDGE CHANNEL CHARACTERISTICS

Channel	ν (GHz)	λ (μm)	Beam FWHM ($''$)	Number of Detectors	NET_{RJ} per detector ($\mu\text{K} \sqrt{\text{s}}$)	σ_{pix} (μK)	$N(> 5\sigma_{\text{pix}})$ (mJy)
L1	150	2000	14	1	68	6.2	79
L2	220	1360	14	1	36	3.3	76
H1	320	940	6	6	91	9.8	99
H2	390	770	6	6	71	7.7	114
H3	480	630	6	6	60	6.5	143
H4	590	510	6	6	49	5.3	176
H5	710	420	6	6	42	4.6	227
H6	870	340	6	6	36	3.9	274
H7	1,060	280	6	6	30	3.3	352
H8	1,290	230	6	6	26	2.8	454
							39

NOTES.—Pixel errors σ_{pix} are for beam-size pixels and observations uniformly covering 1% of the sky over 10 days. The weight-per-unit solid angle of equation (18) is given by $w = 1/(\sigma_{\text{pix}}^2 \text{FWHM}^2)$. For the H (“high-frequency”) channels, we assume only 4 of the six detectors are used. Number of sources observed $N(> 5\sigma_{\text{pix}})$ assumes model E (G98). See <http://topweb.gsfc.nasa.gov> for more details.

We can forecast errors on these parameters by theoretically propagating the measurement errors. This is conveniently done with the Fisher matrix formalism (Kendall & Stuart 1969; Tegmark et al. 1997). In general, the Fisher matrix for a set of parameters, a_p , depends on the covariance matrix of the data (in this case the maps) and the derivatives of the covariance matrix with respect to the parameters:

$$F_{pp'} = \frac{1}{2} \text{Tr} \left[C^{-1} \frac{\partial C}{\partial a_p} C^{-1} \frac{\partial C}{\partial a_{p'}} \right] \quad (16)$$

where the trace here runs over the suppressed indices ℓ, m and ν . Calculating the Fisher matrix is most easily done in spherical harmonic space where the covariance matrix of the maps can be written as

$$C_{\nu lm, \nu' l' m'} \equiv \langle a_{\nu lm} a_{\nu' l' m'} \rangle = c_l^{\nu \nu'} \delta_{ll'} \delta_{mm'} \quad (17)$$

with

$$c_l^{\nu \nu'} \equiv \sum_i C_l^{\nu \nu' (i)} b_\nu(l) b_{\nu'}(l) + w^{-1}(\nu) \delta_{\nu \nu'} \quad (18)$$

where $b_\nu(l)$ is the window function of the beam, $w(\nu)$ is the weight-per-unit solid angle of the map at frequency ν , and the index i labels the various components, which we have assumed to be uncorrelated. Such multi-frequency, multi-component analyses have been performed for CMB experiments by a number of authors (Tegmark & Efstathiou 1996; Bouchet, Gispert & Puget 1996; Knox 1999; Tegmark et al. 2000; Cooray, Hu & Tegmark 2000). We use four components in our modeling: the FIRB correlations, the FIRB shot noise, Milky Way dust, and the CMB. We take the shot noise to be uncorrelated between different frequencies for the sake of simplicity. In reality, the cross-frequency correlations are probably strong. We justify our approximation below.

We can separate the calculation into separate multipoles, so that with uniform coverage over a fraction of

the sky, f_{sky} ,

$$F_{pp'} = \sum_l \frac{(2l+1) f_{\text{sky}}}{2} \text{Tr} \left[c_l^{-1} \frac{\partial c_l}{\partial a_p} c_l^{-1} \frac{\partial c_l}{\partial a_{p'}} \right] \quad (19)$$

where now all the terms in the trace are matrices with (suppressed) indices ν, ν' . When f_{sky} is less than 1, this equation is approximate, although it is generally a very good approximation. The f_{sky} factor accounts for the decreased number of modes available when the sky coverage is less than full.

At this point, the matrices one needs to invert are only size n_{ch} by n_{ch} , where n_{ch} is the number of channels, and therefore this calculation can be done quickly. To simplify the amplitude derivatives, we take them with respect to α_i^2 instead of α_i .

The diagonal element F_{ii} gives the variance on the i^{th} parameter when all the others are being held fixed (the *unmarginalized* case), while the inverse of the Fisher matrix yields the predicted covariance matrix when all parameters are allowed to vary simultaneously (the *marginalized* case). We will also display the results when the amplitudes are allowed to vary but the scale-dependence parameters are held fixed. For all our calculations we restrict the sum in equation (19) to $\ell < 1600$ in order to reduce the dependence of our results on the amplitude of the shot-noise power spectra, which are quite uncertain.

We begin by displaying the predictions for the *EDGE* mission in Figure 8. In the unmarginalized case, the two parameters of the 3 low-redshift bins can be constrained to $\sim 1\%$, while the highest-redshift bin is measured only to $\sim 5\%$. In the marginalized case, all parameters are constrained at the $\sim 10\%$ level. Interestingly, the constraints on the amplitude are very similar whether or not the tilts n_i are allowed to vary. This indicates that the values k_* were well-chosen so that the uncertainties in the amplitudes and tilts are nearly uncorrelated (Eisenstein et al.

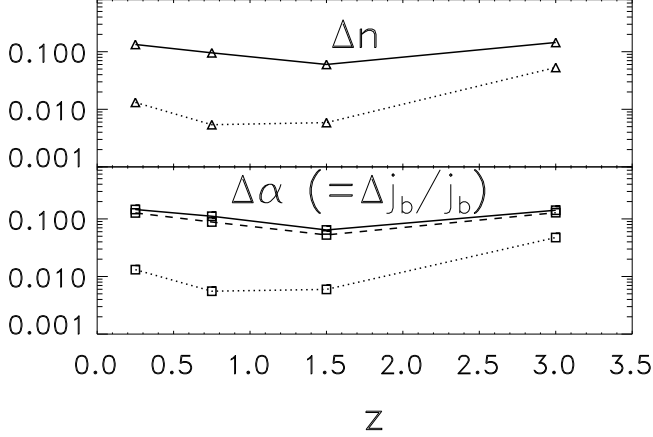


FIG. 8.— Forecasted relative errors from *EDGE* observations on the j_b amplitudes (bottom panel, squares) and absolute errors on the bias spectral index parameters (top panel, triangles) for a model with 8 parameters: the amplitude factor α , and n in 4 redshift bins. Dotted lines connect results for parameter errors assuming the other 7 parameter held fixed. Solid lines connect the results for parameter errors that follow from assuming none of the parameters are fixed. The dashed line shows the result for the amplitude parameters when holding only the n parameters fixed.

1999, for more details, see).

Since *EDGE* is covering 1% of the sky to $\ell \approx 1000$, one would have expected it to yield a $1/\sqrt{0.01 \times 1000^2} = 1\%$ measurement of some combination of these parameters. Indeed, diagonalization of the 4×4 amplitude sub-block of the Fisher matrix shows that this is the case. Table 2 shows that the errors in the fully marginalized case displayed in Figure 8 are dominated by one eigenvalue. Excursions in parameter space that move all of the j_b amplitudes in the same direction are constrained at better than 1%, whereas excursions that move neighboring redshift bins in opposite directions are only constrained to 10%. Indeed, our choice to use only 4 bins constitutes an implicit smoothing prior on the set of all possible excursions of the function $j_b(\nu, z)$, and because the FIRB correlations are projected quantities, one will never constrain highly oscillatory star-formation histories. Physically, of course, such models are absurd. Models that differ by broad, smooth changes can be distinguished by *EDGE* at high accuracy, $\sim 1\%$, which is better than the marginalized errors in Figure 8 would indicate.

We repeat all of the analysis for the *Planck* mission. Since *Planck* covers the full sky, over much of which the dust is a significant contaminant, an accurate treatment of how well *Planck* can measure the α and n parameters of equation (15) would require a more careful treatment of the dust contamination than has been done here. To avoid these complications, we forecast the results for a conservative analysis of the *Planck* data which only uses the cleanest 10% of the sky. We assume that the fluctuation power in this cleanest 10% is the same as assumed for the *EDGE* observations of 1% of the sky.

The results for *Planck* are shown in Figure 9 and Table 2. The behavior is quite similar. The difference between the errors on α_i with and without marginalizing over the n_i are larger in the *Planck* case. This indicates that the α_i and n_i are somewhat correlated. A slightly larger choice for k_*

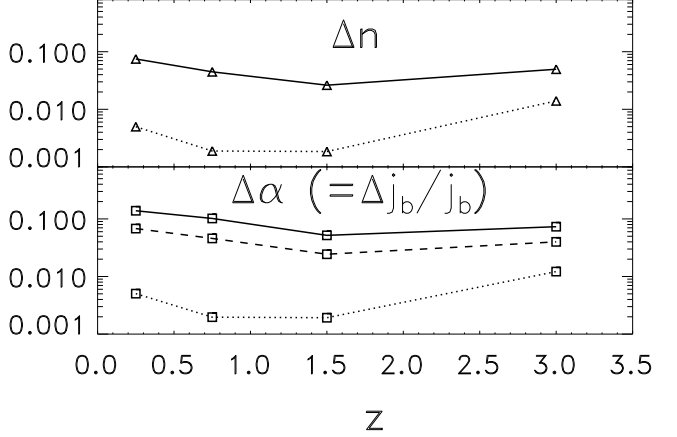


FIG. 9.— Same as Figure 8 but for *Planck*.

would have decorrelated the two sets of parameters, and the errors on α_i would have been simply those in the case where the n_i were not varied. In other words, with a better choice of k_* the amplitude constraints would be quoted as closer to 5% than 10%. The movement of the sweet spot to higher k is a direct result of the greater sensitivity and slightly higher angular resolution of *Planck*.

We have studied the dependence of the parameter errors to changes in experimental parameters and the parameters governing sources of astrophysical noise (namely, the shot noise and dust power spectrum amplitudes). Halving the dust power spectrum makes less than 10% changes in the errors. Increasing it by a factor of 20 makes at most a factor of 2 increase in the parameter errors. Increasing the shot noise power spectrum by a factor of 2 makes less than a 10% change in the errors.

This robustness is fortunate since, as has already been mentioned, our modeling of these contaminants has not been very sophisticated. For the dust we have assumed complete coherence, and for the shot noise complete decoherence; reality for both is somewhere in between. In principle the a_p of equation (16) would be not only the FIRB parameters, but also dust and shot-noise parameters. In effect, our calculation assumes that the $C_l^{\nu\nu'}$ for the dust and shot noise are perfectly known. In reality these statistical properties will have to be determined from the data, although external datasets will provide useful information as well. A further weakness of our dust modeling is the implicit assumption of statistical isotropy. A more rigorous treatment of the dust, which one would need to study FIRB anisotropy in regions of typical dust fluctuation power, would be quite challenging indeed.

Removal of low frequency channels degrades our high- z constraints, as we would expect. Eliminating the *Planck* 217 GHz channel, while not changing the unmarginalized errors, does increase the marginalized errors—in the lowest- z bin by 50% and the highest- z bin by a factor of 2. Removing the three lowest frequency FIRB channels (L2, H1 and H2) has a similar effect. However, simply removing channel L2 makes almost no difference. Presumably the importance of LS would be more readily apparent if the highest- z bin, which runs from $z = 2$ to $z = 4$, were split up more finely. As the bin stands, the H1 and H2

TABLE 2

DIAGONALIZING THE FISHER MATRIX

Experiment	Error on bias $\lambda_F^{-1/2}/2$	Eigenvector			
		$0 < z < 0.5$	$0.5 < z < 1$	$1 < z < 2$	$2 < z < 4$
<i>EDGE</i>	0.0040	0.2799	0.7094	0.6451	0.0471
	0.0151	0.4525	0.4860	-0.7148	-0.2192
	0.0777	0.5798	-0.2458	-0.0380	0.7759
	0.1922	0.6171	-0.4474	0.2673	-0.5896
<i>Planck</i>	0.0014	0.2508	0.6780	0.6884	0.0588
	0.0060	0.4097	0.5361	-0.6469	-0.3554
	0.0234	0.4801	-0.0460	-0.2023	0.8523
	0.0912	0.7340	-0.5008	0.2582	-0.3793

NOTES.—The eigenvalues and eigenvectors of the Fisher matrices for *EDGE* and *Planck*. The scale-dependence parameters n_i have been held fixed here, leaving only the four amplitude parameters α_i . Each row gives an eigenvalue and the corresponding eigenvector. The eigenvalues are listed as the inverse square root of the Fisher matrix eigenvalue λ_F divided by two; this is the $1-\sigma$ error on the bias. The factor of two comes from our use of α_i^2 as a parameter instead of α_i . The eigenvectors specify how that error is divided between the four redshift bins. Note that the spectrum of eigenvalues increases rapidly: model changes that would move all of the biases up or down together are extremely well constrained (better than 1%), whereas changes that shift the biases in alternating fashion are relatively poorly constrained (10-20%).

channels are helping to constrain its amplitude because of their sensitivity to just the lower end of the range.

The high frequency channels are important for separating out the low-redshift contribution from the high-redshift contribution. Removing the highest three frequency channels of *EDGE* has only a small effect on the unmarginalized errors, but the marginalized errors increase by factors of ~ 10 . For *Planck* removal of the 857 GHz channel results in mostly small changes to the unmarginalized errors but factors of from 4 to 8 increase in the marginalized errors.

While frequency range is important, we have not been able to see, with this study, a benefit from a dense sampling of that range, such as offered by *EDGE*. Removing all the even *EDGE* channels (L2, H2, ..., H8) while simultaneously doubling the weight of the odd ones (to keep the total weight roughly unchanged) results in practically no change in either the marginalized or unmarginalized errors. This may be due to the fact that our bins of $1+z$ are coarser than the frequency bins; i.e., the finer the frequency sampling, the faster the changes in emissivity with redshift one should be able to detect. Dense sampling also makes possible more consistency tests and better monitoring of possible dust contamination.

Once again we stress that our results here have assumed small departures around a particular model for the FIRB fluctuations. In particular, it may be possible to have detections of significant emissivity at redshifts beyond 4, if there is such emission. Even if there is not such extra emission, and $\Delta j_b/j_b$ turns out to be large for $z > 4$, one may still be able to set very interesting upper limits on j_b . Combined with a lower limit on the bias, this could be

turned into an upper limit on j_ν alone—providing a new constraint on energy production at high-redshift.

It is now convenient to give some more details on the FIRB power spectrum error forecasts in figure 6. They were the same as the parameter error forecasts described in this section (i.e, equation (16) through equation (19)) with the following changes: (1) for the errors in each panel only two channels were used—the one corresponding to that panel, and the 150 GHz channel as a CMB monitor, (2) the parameters were the FIRB power spectrum multipole moments, $C_l^{\nu\nu}$, instead of the α_i and n_i , (3) dust was ignored, and (4) the FIRB $C_l^{\nu\nu}$ included contributions from non-linear corrections. It should be clear that the figure 6 error forecasts were only used for that figure. They are not an intermediate step in our calculation of FIRB parameter errors.

6. DISCUSSION

The large-angle anisotropies of the FIRB offer a complementary view of the high-redshift universe to that given by direct investigation of far-infrared sources. Clearly, if one could measure the redshift and spectrum of every far-infrared source in some large patch of sky, then one would recover all of the information we have described and more. However, this will not be possible in the near future. By combining high-resolution measurements of the average spectrum and emissivity as a function of redshift with the known statistics of large-scale density fluctuations, the confusion-limited measurement of the FIRB anisotropies gives us a window on the large-scale biasing of the far-infrared sources. In CDM cosmologies, this bias holds implications for the typical mass of the host halo of

the sources (Mo & White 1996), thereby giving an observational window on the halo environment of the starburst and AGN activity that power the FIRB. Theories for how the galaxy density–morphology relation arises (Kauffmann et al. 1993) and why clusters of galaxies form rather than single overmerged galaxies often appeal to there being a preferred mass (or velocity) scale for galaxy interactions (Kolatt et al. 1999; Somerville et al. 2000). If such interactions lead to dust–obscured star formation and nuclear activity, then the bias of the FIRB sources could inform the modeling of bulge and group formation.

It is interesting to compare the limits on clustering that can be gained from confusion–limited measurements to those that could be gained from more typical correlation analyses of sets of individual sources.

First, we will consider the case in which exact redshifts for the sources are known and ask what number and density of sources would be needed to measure the power spectrum over a broad band centered at a comoving wavenumber $k = 0.2h \text{ Mpc}^{-1}$ ($\ell \approx 800$) to $P(k) = 1000h^{-3} \text{ Mpc}^3$ at $k = 0.2h \text{ Mpc}^{-1}$; this corresponds to a bias of 2 at $z \approx 2.5$. For a fixed number of objects N , the power spectrum error bars are minimized when the comoving volume density is equal to P^{-1} (Kaiser 1986; Tegmark 1997a); in this case, the fractional error is approximately $2\sqrt{2}/\sqrt{N \frac{k^3 P(k)}{2\pi^2}}$. Hence, 5% accuracy requires approximately 8000 sources over a comoving volume of $8 \times 10^6 h^{-3} \text{ Mpc}^3$.⁹ If this volume is roughly cubic, then this is approximately a range of 0.25 in redshift and 8 square degrees at $z = 2.5$. If the source density is much smaller or larger than $10^{-3} h^3 \text{ Mpc}^{-3}$, then the number of sources required to achieve a 5% measurement of large-scale power increases dramatically.

Next, we consider the case in which the redshifts are only approximately known, e.g. by using the far–infrared or radio spectral index (Carilli & Yun 1999; Blain 1999e). We approximate this situation by saying that the sources can be divided into a series of redshift slices. Each slice is analyzed by angular correlation methods and is presumed to be statistically independent from the others. In the limit that the conformal distance r changes only slightly across the redshift slice, the angular power spectrum C_ℓ of the sources in the slice is simply the spatial power spectrum at $k = \ell/r$ divided by the comoving volume per steradian in the slice. For $P = 1000h^{-3} \text{ Mpc}^3$ and a slice of unit redshift at $z = 2.5$, this gives $C_\ell \approx 10^{-7}$. The optimal number of sources per steradian to minimize the errors on the measurement of C_ℓ for a given number of sources is simply C_ℓ^{-1} . With this surface density, the fractional errors on C_ℓ are roughly $2\sqrt{2}/\sqrt{N \frac{\ell^2 C_\ell}{2\pi}}$. Inserting $\ell = 800$, one finds a requirement of roughly 3×10^5 sources (in the unit redshift band) spread over 100 square degrees in order to achieve 5% fractional errors on the power spectrum.

In both cases, the amplitude of the power spectrum gives a preferred surface density in a narrow redshift band. This density implies an upper limit to the flux cut of the selection. If we assume that the comoving source density is con-

stant out to $z = 5$ at this flux level, then integrating over redshift implies $\sim 15,000$ total sources per square degree. This corresponds to roughly 1 mJy at $850 \mu\text{m}$ (Hughes et al. 1998). One gets the same answer in either of the two cases above and regardless of the thickness of the redshift slice in the angular analysis; the value is controlled by the amount of volume at high–redshift and the amplitude of the power spectrum one is trying to measure. The detection of sources becomes confusion–limited when the inverse of the source surface density is less than 30 times the beam area. Hence, one can immediately calculate that detecting sources at the density needed to maximize one’s measurement of the high–redshift power spectrum with a fixed number of sources requires a beam smaller than $5''$. Surveys with beams larger than this will reach their confusion limit before achieving the optimal source density and will need to measure more sources in order to gain the same fractional limits on the power spectrum. Surveys with beams smaller than this should not integrate to the confusion–limit but instead cover more sky.

Clearly, resolving the FIRB sources has other benefits with respect to clustering that cannot be matched by a confusion–limited measurement; for example, one can study the clustering of different populations of sources. However, the above calculations show that achieving accuracy equivalent to Figure 8 on the large–scale power spectrum requires large sets of sources: hundreds of thousands with crude redshifts or many thousand with accurate redshifts.

An aspect of the FIRB anisotropies that we have not included in our treatment is the possibility of stochastic bias (Dekel & Lahav 1999). Our assumption that the bias between the emission at different frequencies is perfectly correlated (i.e. that the frequency covariances can be decomposed into $b(\nu)b(\nu')$) is optimistic because it allows measurements of the cross–correlations between frequencies to constrain the j_b directly. However, we find that the HK00 predictions of the cross–correlation differ sufficiently little from perfect correlations that the leverage on the redshift decomposition is relatively weak. Breaking the assumption would slightly weaken our constraints but would also open up a new sector of physical parameters, namely the stochasticity of the relative bias between different frequencies. This can occur if at a given redshift, there are multiple components with differing spectral energy distributions that are imperfectly correlated with each other (and thus necessarily with the density). Such flawed correlations are necessary in the non–linear regime, where the density contrast can’t fall below -1 , but it is unknown whether bias is stochastic on the large scales studied here. If the observed correlation coefficients were more distinct from unity than the baseline predictions, the lack of correlation could be measured and perhaps interpreted. Obviously, it would be intriguing to associate the separate populations with active nuclei versus star formation or quiescent star formation versus starbursts. Hence, the cross–correlations between frequencies could be an interesting route for FIRB anisotropies to constrain the properties of high–redshift sources.

There remains the possibility of truly diffuse emission contributing to the FIRB, i.e., emission which does not resolve into distinct sources. As an example, grey dust

⁹Of course, the required number and volume scale as the inverse square of the desired accuracy; 1% accuracy would require $\sim 200,000$ sources.

distributed throughout the IGM has been invoked as a non- Λ explanation for the anomalously dim high- z supernovae (Aguirre 1999), and it has been shown that if this explanation is correct, then a significant contribution to the FIRB at low frequencies comes from this grey dust (Aguirre & Haiman 2000). We can expect the clustering properties of such emission to be different from that of the individual sources. A cross-correlation analysis of a wide-field map of resolved FIRB sources with a map of the unresolved FIRB emission (as measured by, e.g., *Planck* or *EDGE*) could eventually be used as a probe of any such diffuse component.

7. CONCLUSIONS

We have presented a study of the large-angle clustering properties of the far-infrared background, focusing on the role of confusion-limited anisotropy experiments. We find that under reasonable assumptions, and in regions of the sky with unusually low Galactic dust emission, correlated FIRB fluctuations should dominate the observed angular power spectrum over a wide range of frequencies and angular scales. As a result, such experiments will provide useful constraints on any model for the sources of the FIRB. The main drawback of the confusion-limited technique is that it cannot easily separate different physical classes of sources, and so many important questions about the nature and distribution of far-infrared sources will remain squarely in the domain of high-resolution studies. However, matching the constraints on the large-scale clustering that could be produced by the *EDGE* or *Planck* experiments requires an impressively large set of point source measurements with or without accurate redshift information.

To model the FIRB fluctuations, one must specify the spectrum, emissivity, and bias of high-redshift galaxies and AGN, as well as the redshift evolution of these quantities. Despite the inherent degeneracies, we find that confusion-limited anisotropy observations yield tight constraints on certain combinations of these model ingredients. Without external spectral information, the emissivity is degenerate with the temperature of the sources. However, as the plausible ranges of temperatures and biases are reasonably small, the FIRB anisotropies by themselves could detect strong variations in the emissivity as a function of redshift, notably the turn-on of embedded star formation at high redshift. We find that if the mean emission spectrum was precisely known, the bias-weighted emissivity could be measured to $\sim 10\%$; while strong priors on the amount of oscillation allowed as a function of redshift can allow these constraints to approach 1%. These constraints are tighter than differences between possible models for the sources of the FIRB, rendering such studies of the infrared sky a useful probe of the high-redshift universe.

We thank S. Meyer, W. Hu, and M. Zaldarriaga for many useful conversations, J. L. Puget for pointing out how much the dust power spectrum varies spatially, and D. Finkbeiner for assistance with the WOMBAT dust and synchrotron predictions. LK is supported by the DOE, NASA grant NAG5-7986 and NSF grant OPP-8920223. DJE and ZH were supported by NASA through Hubble

Fellowship grants #HF-01118.01-99A and #HF-01119.01-99A from the Space Telescope Science Institute, which is operated by the Association of Universities for Research in Astronomy, Inc, under NASA contract NAS5-26555. AC acknowledges support from J. Carlstrom, W. Hu, and D. York.

REFERENCES

Adelberger, K. L., Steidel, C. C., Giavalisco, M., Dickinson, M., Pettini, M., & Kellogg, M. 1998, *ApJ*, 505, 18
 Aguirre, A., 1999, *ApJ*, 525, 583
 Aguirre, A., & Haiman, Z. 2000, *ApJ*, 532, 28
 Barger, A. J., Cowie, L. L., Sanders, D. B., Taniguchi, Y. 1998, *Nature*, 394, 248
 Barger, A. J., Cowie, L. L., & Sanders, D. B., 1999a, *ApJ*, 518, L5
 Barger, A. J., Cowie, L. L., Smail, I., Ivison, R. J., Blain, A. W., & Kneib, J.-P. 1999b, *AJ*, 117, 2656
 Baugh, C. M., Benson, A. J., Cole, S., Frenk, C. S., & Lacey, C. G. 1999, *MNRAS*, 305, L21
 Blain, A. W., Jameson, A., Smail, I., Longair, M. S., Kneib, J.-P., & Ivison, R. J. 1999a, *MNRAS*, 309, 715
 Blain, A. W., Kneib, J.-P., Ivison, R. J., & Smail, I. 1999b, *ApJ*, 512, L87
 Blain, A. W., Smail, Ivison, R. J., & Kneib, J.-P. 1999c, *MNRAS*, 302, 632
 Blain, A. W. 1999d, *astro-ph/9906141*.
 Blain, A. W. 1999e, *MNRAS*, 309, 955
 Blanton, M., Cen, R., Ostriker, J. P., Strauss, M. A., & Tegmark, M. 2000, *ApJ* 531, 1
 Bond, J. R., Carr, B. & Hogan, C. 1986, *ApJ* 306, 428
 Bouchet, F.R., Gispert, R. & Puget, J.L. 1996, in *AIP Conf. Proc. 348: Unveiling the Cosmic Infrared Background*, ed. E. Dwek (Baltimore: AIP), 225
 Bunn, E., & White, M. 1997, *ApJ*, 480, 6
 Carilli, C. L., & Yun, Min S. 1999, *ApJ*, 513, L13
 Carlstrom, J. 2000, private communication
 Cooray, A., Hu, W., Tegmark, M. 2000, *ApJ* in press (*astro-ph/0002238*)
 de Bernardis, P., Ade, P. A. R., Artusa, R. et al. 1999, *New Astronomy Reviews*, 43, 289
 de Bernardis, P. et al., 2000, *Nature* 404, 955 (*astro-ph/0004404*)
 de Oliveira-Costa, A. & Tegmark M., 1999, *Microwave Foregrounds (ASP: San Francisco, 1999)*
 Dekel, A., & Lahav, O. 1999, *ApJ*, 520, 24
 Draine, B. T., & Lee, H. M. 1984, *ApJ*, 285, 89
 Dwek, E., et al. 1998, *ApJ*, 508, 106
 Eales, S., Lilly, S., Gear, W., Dunne, L., Bond, J. R., Hammer, F., Le Fevre, O., & Crampton, D. 1999, *ApJ*, 515, 518
 Efstathiou, A., Oliver, S., Rowan-Robinson, M. 2000, *MNRAS* in press (*astro-ph/0008065*)
 Eisenstein, D. J., & Hu, W. 1999, *ApJ*, 511, 5
 Eisenstein, D. J., Hu, W., & Tegmark, M., 1999, *ApJ*, 518, 2
 Finkbeiner, D. P., Schlegel, D.J., Davis, M., 1999, *ApJ* 524, 867
 Fixsen, D. J., et al. 1998, *ApJ*, 508, 123
 Frayer, D. T., Ivison, R. J., Scoville, N. Z., Evans, A. S., Yun, M. S., Smail, Ian, Barger, A. J., Blain, A. W., & Kneib, J.-P. 1999, *ApJ*, 514, L13
 Gautier, T.N.I., Boulanger, M., Perault, M. & Puget, J.L. 1992, *AJ*, 103, 1313
 Giavalisco, M., Steidel, C. C., Adelberger, K. L., Dickinson, M. E., Pettini, M., & Kellogg, M. 1998, *ApJ*, 503, 543
 Gispert, R., Lagache, G., Puget, J. L. 2000, *A&A*, 360, 1
 Glenn, J., et al. 1998, *Proc. SPIE*, 3357, 326
 Gnedin, N., & Ostriker, J. 1996, *ApJ*, 486, 581
 Guiderdoni, B., Hivon, E., Bouchet, F. R., & Maffei, B. 1998, *MNRAS*, 295, 877
 Haiman, Z. & Knox, L. 2000, *ApJ*, 530, 124
 Haiman, Z., Abel, T. & Rees, M. 2000, *ApJ*, 534, 11
 Hanany, S. et al., submitted to *ApJ* (*astro-ph/0005123*)
 Holland, W. S., et al. 1998, *Nature*, 392, 788
 Hughes, D., et al. 1998, *Nature*, 398, 241
 Jaffe, A. H. et al., submitted to *Phys. Rev. Lett.* (*astro-ph/0007333*)
 Jimenez, R., & Kashlinsky, A. 1997, *ApJ*, 511, 16
 Kaiser, N., 1986, *MNRAS*, 219, 785
 Kashlinsky, R. & Odenwald, S., 2000, *ApJ*, 528, 74
 Kauffmann, G., White, S. D. M., Guiderdoni, B., 1993, *MNRAS*, 264, 201
 Kendall, M. G. & Stuart, M. G., 1969, *The Advanced Theory of Statistics*, Vol. II (London: Griffin)
 Knox, L. 1999, *MNRAS*, 307, 977

Kollat, T. S., Bullock, J. S., Somerville, R. S., Sigad, Y., Jonsson, P., Kravtsov, A. V., Klypin, A. A., Primack, J. R., Faber, S. M., & Dekel, A. 1999, ApJ, 523, L109

Lagache, G., Abergel, A., Boulanger, F., Désert, F. X., Puget, J.-L. 1999, A&A, 344, 322

Lagache, G. & Puget, J. L., 2000, A&A, 355, L17

Limber, D. N. 1953, ApJ 117, 134

Madau, P. 1997, in *Star Formation Near and Far : Seventh Astrophysics Conference*, Eds. Steven S. Holt and Lee G. Mundy, Woodbury N. Y. : AIP Press; AIP Conf. Ser., 393, 481

Madau, P., Pozzetti, L., Dickinson, M. 1998, ApJ, 498, 106

Madau, P. 1999, in *Physica Scripta, Proc. of the Nobel Symposium "Particle Physics and the Universe"*, held at Enkoping, Sweden, August 20-25, 1998, in press, preprint astro-ph/9902228.

Mather, J.C., Fixsen, D.J. and Shafer, R.A., 1993, Proc. SPIE, 2019, 168 (SPIE: Bellingham, WA)

Mo, H. J., & White, S. D. M. 1996, MNRAS, 282, 347

Oliver, S., Rowan-Robinson, M., Alexander, D. M. 2000, MNRAS, 316, 749

Peebles, P. J. E. 1980, *Large-Scale Structure of the Universe*, Princeton Univ. Press

Perlmutter, S., & Riess, A. 1999, in proceedings of "COSMO-98", Second International Workshop on Particle Physics and the Early Universe, Ed. D.O. Caldwell, AIP Conference Proceedings, vol. 478., American Institute of Physics Press, Woodbury, NY, p.129

Puget, J. L. et al. 1996, A&A, 308, L5

Puget, J. L., Lagache, G., Clements, D. L. et al. 1999, A&A, 345, 29

Smail, I., Ivison, R. J., & Blain, A. W. 1997, ApJ, 490, L5

Smail, I., Ivison, R., Blain, A. and Kneib, J.-P. 2000, preprint astro-ph/0008237

Schlegel, D.J., Finkbeiner, D. P., Davis, M., 1998, ApJ 500, 525

Serjeant, S., Oliver, S., Rowan-Robinson, M. 2000, MNRAS 316, 768

Somerville, R. S., Primack, J. R., Faber, S. M. 2000, MNRAS, in press; astro-ph/0006364

Stecker, F. W., Puget, J.-L. & Fazio, G. G. 1977, ApJ 214, 51L

Steidel, C. C., Adelberger, K. L., Dickinson, M., Giavalisco, M., Pettini, M., & Kellogg, M. 1998, ApJ, 492, 428

Tegmark, M. & Efstathiou, G. 1996, MNRAS, 281, 1297

Tegmark, M. 1997a, Phys. Rev. Lett., 79, 3806

Tegmark, M., Taylor, A. N. & Heavens, A. F., 1997b, ApJ, 480, 22

Tegmark, M. & de Oliveira-Costa, A. 1998, ApJ, 500, L83

Tegmark, M., Eisenstein, D. J., Hu, W., & de Oliveira-Costa, A. 2000, ApJ, 530, 133

Viana, P. T. P., & Liddle, A. R. 1999, MNRAS, 303, 535

Wright, E. L. 1998, ApJ, 496, 1